ACTUATORS

Bistable soft jumper capable of fast response and high takeoff velocity

Daofan Tang[1,2]†, Chengqian Zhang[1,3]*†, Chengfeng Pan[1,2], Hao Hu[1,2], Haonan Sun[1,2], Huangzhe Dai[1,2], Jianzhong Fu[1,2], Carmel Majidi[4]*, Peng Zhao[1,2]*

In contrast with jumping robots made from rigid materials, soft jumpers composed of compliant and elastically deformable materials exhibit superior impact resistance and mechanically robust functionality. However, recent efforts to create stimuli-responsive jumpers from soft materials were limited in their response speed, takeoff velocity, and travel distance. Here, we report a magnetic-driven, ultrafast bistable soft jumper that exhibits good jumping capability (jumping more than 108 body heights with a takeoff velocity of more than 2 meters per second) and fast response time (less than 15 milliseconds) compared with previous soft jumping robots. The snap-through transitions between bistable states form a repeatable loop that harnesses the ultrafast release of stored elastic energy. On the basis of the dynamic analysis, the multimodal locomotion of the bistable soft jumper can be realized: the interwell mode of jumping and the intrawell mode of hopping. These modes are controlled by adjusting the duration and strength of the magnetic field, which endows the bistable soft jumper with robust locomotion capabilities. In addition, it is capable of jumping omnidirectionally with tunable heights and distances. To demonstrate its capability in complex environments, a realistic pipeline with amphibious terrain was established. The jumper successfully finished a simulative task of cleansing water through a pipeline. The design principle and actuating mechanism of the bistable soft jumper can be further extended for other flexible systems.

INTRODUCTION

Many organisms, ranging from insects to fish, use jumping as a means of locomotion, hunting, or evading predators (*1*, *2*). For example, a grasshopper can leap about 10 times its body length in a vertical jump or 20 times its length horizontally using its muscular hind legs (*3*). Unlike other modes of locomotion, such as crawling or rolling, jumping has proved to be highly efficient and adaptable to complex terrain and has gained notable attention for potential applications in the field of miniaturized robotics (*4*–*8*).

Progress has been made in recent years to adopt jumping locomotion soft robots that are capable of large elastic deformations, high impact resistance, and durable and mechanically robust functionality. These include a series of soft jumping robots based on various actuating methods, including dielectric elastomers (*9*–*11*), liquid crystal elastomers (*12*–*15*), combustion (*16*, *17*), and soft fluidic actuators (*18*–*20*).

However, existing soft jumping robots still cannot compete with natural organisms in jumping capabilities. Because of the low modulus and compliance of soft materials, it is still challenging to design a soft robot to achieve both excellent jumping performance and high flexibility, especially at small-length scales. The first challenge comes from the requirement for high power output during jumping. The actuating forces of most soft robots come from the stimulus sources because the stimulus sources directly actuate the soft materials, causing them to mimic the contraction and relaxation of muscles in nature. Soft robots can perform movements, such as rolling (*21*–*23*), walking (*19*, *24*), crawling (*25*–*27*), and swimming (*28*, *29*), through interactions between the actuating force and the surrounding environment. Typical of these is the insect-scale fast-moving robot based on piezoelectricity (*30*). It can achieve rapid movement with a high driving frequency (approximately 850 Hz) using a single driver with relatively low power. However, when it comes to jumping, the actuating forces provided by the stimulus sources cannot satisfy the requirement of generating considerable power to achieve a high takeoff velocity. Nonetheless, notable advancements have been made in achieving high power output by storing a large amount of energy, primarily strain energy for soft robots, and releasing it when necessary. This mechanism can be classified as power amplification. Such power-amplified systems typically use a latch-spring system or snap-through instability. For the latch-spring system, which is commonly used in rigid robots, the elastic potential energy can be accumulated in the system and converted to kinetic energy upon release of the latch. For soft robots, the integration of a latch in the flexible system [such as magnets (*12*, *18*), adhesives (*13*, *31*), or locking parts (*14*)] is necessary to avoid unexpected release during elastic loading, which adds complications for the overall system. In addition, after completing a jump, the introduced latch needs to be reset to prepare for the next jump, which greatly increases the pulse interval time and impedes the continuous jumping of the soft robot. Different from the latch-spring system, snap-through instability relies on the snap-through mechanism to realize rapid energy release. By harnessing the structural instability, it is possible to design and construct a system in which a small amount of stimulus can trigger instantaneous spikes in energy (*32*, *33*). In this prospect, the buckling instability stands out as a promising strategy for designing soft jumping robots.

The second challenge arises from the design of the robot's jumping mechanism to achieve efficient locomotion including a fast response

[1]State Key Laboratory of Fluid Power and Mechatronic Systems, College of Mechanical Engineering, Zhejiang University, Hangzhou 310027, China. [2]Key Laboratory of 3D Printing Process and Equipment of Zhejiang Province, College of Mechanical Engineering, Zhejiang University, Hangzhou 310027, China. [3]Center for X-Mechanics, Department of Engineering Mechanics, Zhejiang University, Hangzhou 310027, China. [4]Soft Machines Lab, Department of Mechanical Engineering, Carnegie Mellon University, Pittsburgh, PA 15213, USA.
*Corresponding author. Email: zhangcq@zju.edu.cn (C.Z.); cmajidi@andrew.cmu.edu (C.M.); pengzhao@zju.edu.cn (P.Z.)
†These authors contributed equally to this work.

and short pulse interval time. At present, a popular method for actuating soft jumping robots is to use light-driven liquid crystal elastomers (*13*, *14*, *34*). However, for these systems, it is time-consuming both for the stimuli generated by the photothermal effect and for the passive cooling required to recover from the heated state. As an alternative, magnetic actuation can be used in soft robotics to facilitate complex motions with a rapid response (*35*) because the embedded magnetic particles of materials tend to align with the magnetic field immediately once the magnetic field is applied (*36*, *37*). Moreover, the magnetic field can penetrate through a wide range of materials, which has been widely used in the actuation of soft robots for working in confined environments (*38*). Considering soft jumping robots' requirements, magnetic actuation is an appealing choice for powering a high-performance yet flexible soft jumping robot.

Numerous attempts have been made to use snap-through instability to achieve notable deformation and rapid actuation in magnetic systems (*39*–*42*). Researchers have succeeded in using a magnetic slender beam with two fixed ends to achieve rapid transitions between different stable states. The snap-through behavior has been predicted through theoretical models, which confirms the feasibility of combining magnetic actuation and buckling instability systems and their superiority in actuation efficiency. However, the dynamics of the snap-through transition coupled with magnetic actuation in building a magnetic-driven soft system remains unexplored. Most modeling work focuses on the static or quasistatic analysis of the snap-through behavior. In addition, to enhance maneuverability, the soft jumping robot needs to integrate multimodal locomotion to adapt to different scenarios (*43*), which poses challenges to the structural design and actuating mode.

Here, we propose an ultrafast bistable soft jumper driven by a magnetic field that balances robust jumping capability and jumping maneuverability. To the best of our knowledge, the proposed bistable soft jumper is advanced in both the jumping capability (jumping more than 108 body heights with a takeoff velocity of more than 2 m/s) and the response time (less than 15 ms) compared with existing soft jumping robots (table S7). The bistable soft jumper incorporates a bistable structure that uses a snap-through transition to rapidly release energy and perform jumping. The snap-through transitions between two stable states can be instantaneously triggered by an external magnetic field because the energy storage and the energy release for jumping are integrated within the bidirectional deformation of the bistable structure. A large amount of potential energy can be stored in the form of elastic strain and converted into kinetic energy for launching upward. We not only performed the static analysis to predict the snap-through transition of the bistable soft jumper but also built a dynamic model to analyze the dynamic response of the bistable soft jumper under the magnetic field. On the basis of the dynamic analysis, the multimodal locomotion of the bistable soft jumper can be realized: the interwell mode of jumping and the intrawell mode of hopping. Furthermore, the bistable soft jumper is capable of 360° omnidirectional jumping, and the jumping trajectories can be adjusted in height and distance. We demonstrated these capabilities of the bistable soft jumper within a curved pipe that was partially filled with fluid. In this demonstration, the jumper can move through the confined space of the pipe and cleanse the standing water within the pipe through the release of a chemical agent.

RESULTS

Magnetic-driven bistable soft jumper

Referring to the image in Fig. 1A, the bistable soft jumper was composed of nonmagnetic and magnetized elastomers and was shaped into a pyramid-like folding structure that could be configured to point up or down. This three-dimensional structure was supposed to maintain two stable states on the basis of the variation of internal potential energy. As shown in Fig. 1B, stable state 1 corresponded to the unstrained configuration of the structure, where the internal potential energy of the system remained zero. Stable state 2 corresponds to the configuration of the structure stabilized in the energy barrier of the internal potential energy. In this state, θ is the flapping angle of the bistable soft jumper, which is defined as the angle between the magnetic panel and the ground. During the transition from stable state 1 to stable state 2, the creases underwent stretching and bending because of the magnetic torque T of the adjacent magnetic materials. The internal potential energy ($E_{\text{potential}}$) of the structure sharply increased during the deformation process, and after reaching the peak, it decreased to form an energy barrier that was referred to as stable state 2. When the structure stabilized to stable state 2, a large amount of energy was stored because of the elastic strain of creases. By the same token, when the structure reversed from stable state 2 back to stable state 1, the stored potential energy could be quickly released through snap-through instability and converted into kinetic energy for jumping. On the basis of this mechanism, two different materials were applied to build the bistable structure. The magnetic panels of the structure, which contained NdFeB (neodymium iron boron) ferromagnetic particles with an average diameter of 5 μm (75 wt %), served as the actuating parts. The four magnetic panels were magnetized to align the polarities of NdFeB ferromagnetic particles. After magnetization, the magnetic panels had the same resident magnetization direction, enabling them to undergo flipping under the influence of an external magnetic field, thereby actuating the deformation of the whole structure. The creases were composed of silica gels [a mixture of Ecoflex silicone and polydimethylsiloxane (PDMS)] and acted as the elastically deformable portions of the structure. Compared with the magnetic panels of the structure, the creases had a smaller modulus, which made them easier to bend and stretch. The creases could store or release a large amount of strain potential energy during the transition between stable states.

The jumping mechanism presented here allowed for consecutive cycles of energy storage and release, forming a loop that could be controlled by the magnetic field. Moreover, the overall duration of the magnetic-driven loop could be as short as about 15 ms. With this mechanism, the soft jumper could jump as high as more than 100 times its body height (Fig. 1C and movie S1). In Fig. 1D, we compared the jumping height of our bistable soft jumper with that of other soft jumpers. The y axis represents the height ratio, which is the ratio of jumping height to body height. Body height is defined as the maximum vertical length of the body that the jumper can maintain throughout the actuation process. Using this metric allows for a fair comparison of jumping performance because jumping is primarily a vertical motion. The comparison indicated that the proposed bistable soft jumper could achieve a higher jumping height while maintaining a relatively small size; this advantage rendered the bistable soft jumper particularly well suited for environments such as pipelines, where the space is limited and the height variations are large. Furthermore, the soft jumpers were compared on the basis of

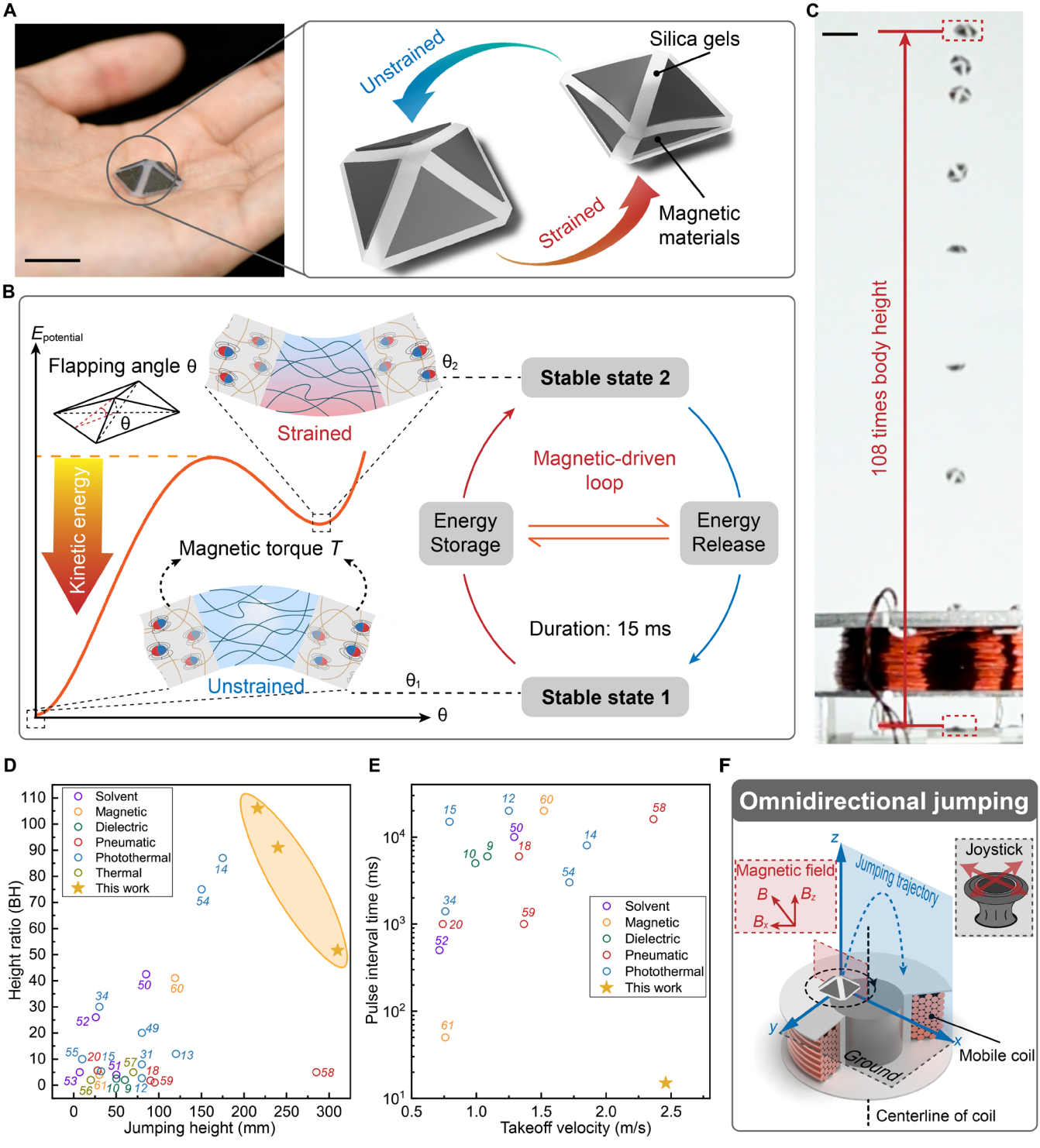

Fig. 1. Schematic illustration of bistable soft jumper. (**A**) Image of the proposed bistable soft jumper and its construction. (**B**) Mechanism of the bistable soft jumper as a magnetic-driven loop including energy storage and energy release. The *x* axis is the flapping angle, and the *y* axis is the internal potential energy. (**C**) An overlaid image indicating the maximum jumping height (108 times body height) of the bistable soft jumper. (**D**) A comparative summary of the jumping height and height ratio of soft robots reported in the literature and this work, including solvent (*50*–*53*), photothermal (*12*–*15*, *31*, *34*, *49*, *54*, *55*), thermal (*56*, *57*), pneumatic (*18*, *20*, *58*, *59*), dielectric (*9*, *10*), and magnetic (*60*, *61*) soft robots. BH, body height. (**E**) A comparative summary of the takeoff velocity and pulse interval time of soft robots reported in the literature and this work. (**F**) Schematic of omnidirectional jumping. Scale bars, 10 mm.

their pulse interval time and takeoff velocity (Fig. 1E) because most soft jumpers face a trade-off between pulse interval time and takeoff velocity. For example, a long time for energy storage is needed to accumulate energy for achieving a high takeoff velocity. The bistable soft jumper overcame this trade-off through the use of a bistable structure that could be actuated repeatedly by the magnetic field, allowing it to achieve rapid takeoff velocities while requiring a very short pulse interval time. In addition to the aforementioned metrics, the bistable soft jumper exhibited a high degree of controllability, as shown in Fig. 1F. The relationship between the magnetic field and the jumping trajectory was established. The bistable soft jumper could realize omnidirectional jumping under the guidance of the magnetic field. To facilitate practical use, a joystick was used to adjust the relative position of the electromagnetic coil and the bistable soft jumper, thereby adjusting the magnetic field in space. This allowed for precise adjustment of the bistable soft jumper's jumping height and distance.

Analysis of the bistable structure

To further understand the overall deformation process of the bistable soft jumper and analyze the formation mechanism of the second stable state, a finite element analysis (FEA) was conducted on the bistable soft jumper with the help of the commercial software ABAQUS (*37*). Here, each magnetic panel had a programmed magnetization **M** with the same direction. The Helmholtz coil was applied to generate a uniform magnetic field for actuation (Supplementary Methods). In the presence of a uniform magnetic field **B**, the magnetic torque T was generated as follows:

$$T = |V(\mathbf{M} \times \mathbf{B})| \tag{1}$$

The magnetic torque tends to rotate the magnetic panel to align the direction of **M** with the direction of **B**. The bistable soft jumper was composed of silica gels and magnetic materials. The material parameters, including Young's modulus, shear modulus, bulk modulus, magnetization, and applied magnetic field, were specified in the input file. The process of deformation was simulated (Fig. 2A), during which it could be observed that the structure underwent stretching and bending and that the majority of the strain (the maximum principal strain) was concentrated in the creases. To verify the accuracy of the simulation, the length-to-height ratio of the actual deformation was compared with that of the simulated deformation. As illustrated in Fig. 2B, the height change during deformation is represented by Δx, and the length change is represented by ΔL. The linear regression analysis of the length-to-height ratio is shown in Fig. 2C. The linear regression curve (blue dashed line) assumed that the simulated values were equal to the experimental values. The root mean square error (RMSE) between the actual values and predicted results was about 0.1482, which indicated that the simulation of deformation was in good agreement with the actual deformation. The small deviation could still be observed when crossing the critical point (Fig. 2B). Although the simulation was a quasistatic process, the actual deformation was a dynamic process. In addition, the boundary conditions we set in the simulation were simplified compared with the actual situation, which caused the length-to-height ratios to deviate from the ideal values. The deformation of the materials brought fluctuations to the elastic potential energy of the structure. Under certain combinations of parameters, an energy barrier formed during the deformation process, which created a second stable state besides the initial state. Considering that most of the deformation occurred at the creases of the structure, a simplified theoretical model (Supplementary Methods) (*44*) was derived to calculate the strain of the creases during the deformation of the structure with the help of geometric analysis. The strain energy of creases could be divided into stretching strain energy and bending strain energy

$$E_{\text{stretching}} = \frac{2EtS^3}{3w_0}\left(\sin\frac{\varphi}{2} - \sin\frac{\varphi_0}{2}\right)^2 \tag{2}$$

$$E_{\text{bending}} = \frac{ESt^3}{24w_0}\left(\gamma - \gamma_0\right)^2 \tag{3}$$

where E is the Young's modulus of the material, t is the thickness of the crease, S is the length of the crease, w_0 is the original width of the crease, and φ and γ are defined as the stretching angle and bending angle of the crease, respectively. The theoretical analysis allowed us to investigate the influences of structural parameters on the potential energy curve.

We quantitatively analyzed the influences of parameters on the stretching energy and bending energy. According to the theoretical analysis, the stretching stress initially increased and then decreased once the deformation crossed the critical point. In contrast, the bending strain continued to increase as the deformation progressed. The superposition of stretching strain and bending strain shaped the final trend of the energy curve. It can be observed from Fig. 2D that the structural height of the sample had a direct effect on the formation of the second stable state. As the structural height increased, the stretching strain obtained more notable gains than the bending strain. Considering the changing characteristics of bending strain and stretching strain, the peak of the potential energy curve appeared near the critical point to generate an energy barrier, which transformed the whole structure from a monostable state to a bistable state. The theoretical predictions and simulation curves matched very well in relating the potential energy and flipping angle. Besides potential energy, the bistable feature could also be characterized by torque during the deformation. As shown in Fig. 2E, the internal torque of the structure increased along with the rise in structural height because the structure with higher structural height became stiffer. The bistable structure had a quite different torque variation curve from the monostable structure: If there existed a second stable state in the structure, then the internal torque of the bistable structure would first increase and then decrease to the negative value, whereas the internal torque of the monostable structure did not decrease to the negative value. The positive value of the torque meant that the monostable structure would always return to the initial state in which the driving torque disappeared. To actuate the deformation by the magnetic field, the magnetic torque generated by the magnetic field needed to be no less than the internal torque of the structure during the deformation. The magnetic torque increased and then decreased during the deformation, and the peak of the magnetic torque occurred when the magnetization of the magnetic panel was perpendicular to the direction of the magnetic field (Supplementary Methods). We first measured the critical magnitude of the magnetic field that could trigger the snap-through transition in the experiment and then obtained the critical magnetic torque based on Eq. 1. The measured critical magnetic torque agreed well with the maximum internal torque obtained from the simulation.

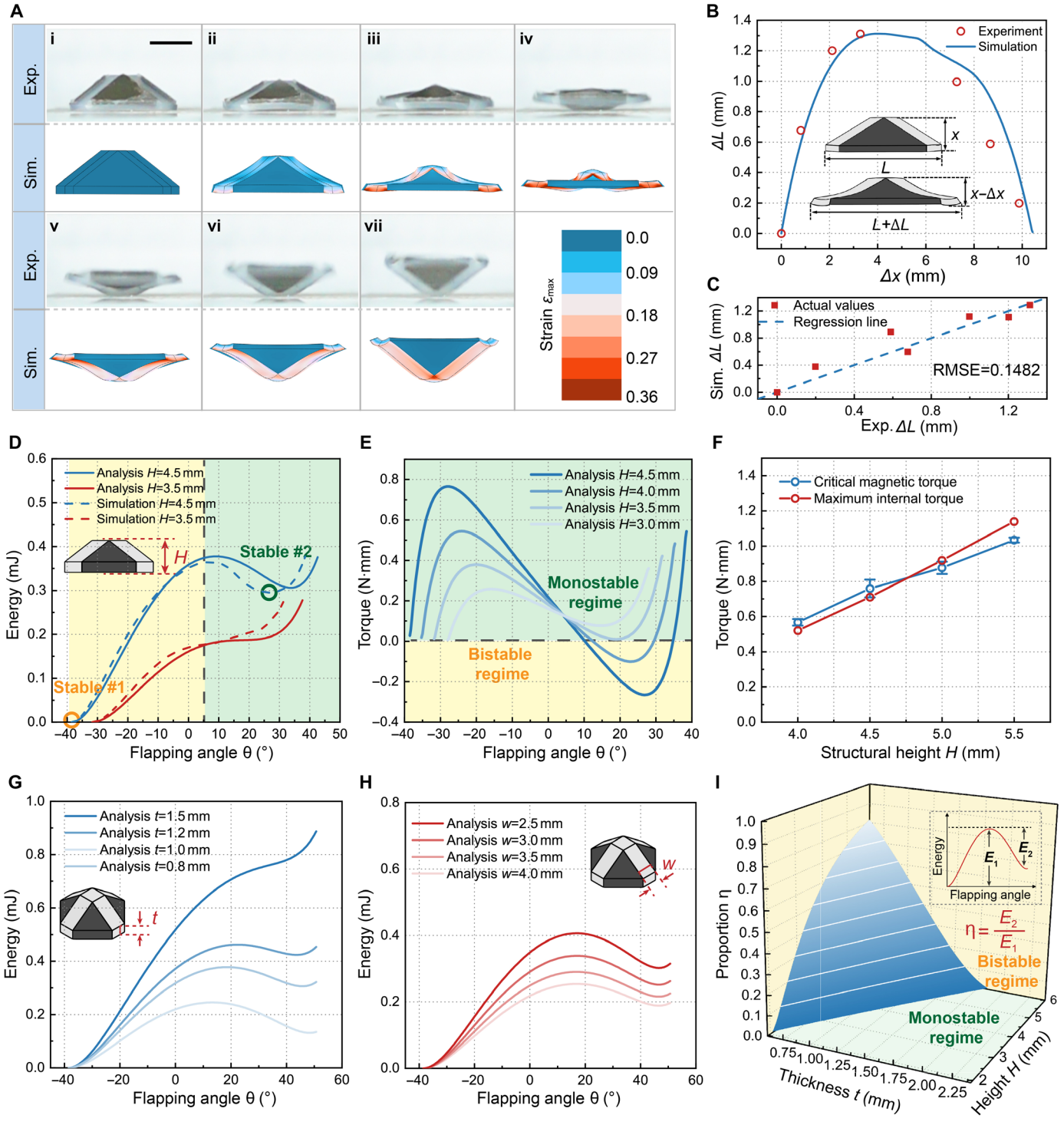

Fig. 2. Mechanisms of the bistable structure. (**A**) FEA verification of the deformation process of the bistable structure. Scale bar, 10 mm. (**B**) Comparison of the experiment and simulation on the length-to-height ratio. (**C**) Linear regression analysis for the length-to-height ratio of the experiment and simulation based on the RMSE. (**D**) Simulated and calculated energy of structures with different structural heights as a function of θ. (**E**) Calculated torque of structures with different structural heights as a function of θ. (**F**) Comparison of the measured critical magnetic torque with the maximum internal torque of the simulation. Error bars represent SD ($N = 3$). (**G**) Influences of different crease thicknesses on the energy of bistable structures. (**H**) Influences of different crease widths on the energy of bistable structures. (**I**) Parameter map illustrating the influences of crease thickness and structural height on the proportion of energy barrier; the results were obtained from the analytical model.

In addition, we analyzed the influences of crease width w and crease thickness t on the overall energy curves. The excessive thickness greatly promoted the transformation of the system from bistability to monostability (Fig. 2G), whereas the crease width had less effect on the bistable characteristic (Fig. 2H). Furthermore, we defined the proportion $\eta = E_2/E_1$ to evaluate the energy barrier of each bistable structure, where E_1 represents the peak of potential energy and E_2 represents the energy barrier between the peak and the energy of the second stable state. A larger value of η represents a deeper energy barrier that improves the robustness of the bistability, but it might not be beneficial for jumping because it implies that a larger magnetic field is required for triggering jumping. Figure 2I reveals the combined influences of the structural height H and crease thickness t on the proportion η. In the landscape map, for each H, there was a critical crease thickness t that promoted the system to be bistable. The depiction of multiple parameters' influences made it feasible to select appropriate parameters to design the bistable structure and tune the internal energy barrier for the soft jumper. For the additional experiments, a structural height H of 6 mm, a crease width w of 3 mm, and a crease thickness t of 1 mm were selected for the standardized parameters of the bistable soft jumper to achieve a balance between energy storage and bistability robustness.

Analysis of dynamic characteristics of the bistable soft jumper

In addition to static mechanics analysis, we also conducted a dynamic analysis of the bistable soft jumper. As a snap-through system, the bistable soft jumper maintained either stable state 1 or stable state 2, with no intermediate state being energetically admissible. We found that the shift between two stable states was related not only to the strength of the magnetic field but also to its duration. Experiments were conducted to confirm the following hypothesis: As the strength of the magnetic field increases, the duration of the magnetic field required to realize the transition decreases. However, if the strength of the magnetic field is reduced, then the required actuating time of the magnetic field will increase correspondingly, until the point at which the transition of the stable states becomes perpetually unachievable. In other words, each bistable structure has a critical strength of the magnetic field for transformation. Figure 3A illustrates the parameters required for the shift from stable state 2 to stable state 1. To further explain the experimental results, the three-dimensional structure of the bistable soft jumper was simplified into a two-dimensional model, which was analyzed as the von Mises truss (*45*, *46*) for the mechanical dynamic analysis (Supplementary Methods). The theoretical model established the relationship between the critical strength of the magnetic field and the duration of the magnetic field. On the basis of the theoretical derivation, the strength of the magnetic field needed for snap-through transition decreased as the duration extended, eventually approaching the critical value infinitely as the duration increased. The theoretical line represented the critical magnetic field for triggering the snap-through transition of the bistable soft jumper, which was in good agreement with the experimental results. On the basis of the critical line of the parameter map, we separated the deformation of the bistable soft jumper into two modes: the interwell mode and the intrawell mode.

For the intrawell mode that was below the critical line, the bistable soft jumper underwent deformation but failed to trigger the snap-through transition. When the magnetic field ceased, the bistable soft jumper recovered to its initial state. A small amount of potential energy was stored and released in the intrawell mode, which could only slightly lift the robot off the ground. When we applied a high-frequency alternating magnetic field, the bistable soft jumper continuously jumped with relatively low jumping heights, which we called hopping (Fig. 3, B and C). Although hopping could not overcome large obstacles because of height limitations, it supported highly controllable locomotion with slight and precise displacements per actuating cycle, which was a valuable complement to the interwell mode of jumping.

For the interwell mode, the bistable soft jumper underwent a rapid and intense snap-through buckling. To further understand how the bistable soft jumper transformed from the stable state to ultrafast jumping within milliseconds, we recorded the entire actuating process using a camera at 10,000 frames per second (movie S2). We specifically calculated the instantaneous velocities at the center and edge of the bistable soft jumper (Fig. 3D), and it was found that the bistable soft jumper underwent a marked energy conversion from potential energy into kinetic energy. From this measurement, it was shown that the velocity at the center reached its maximum value (about 3.5 m/s) from zero when crossing a critical point in a time of t_0 (Fig. 3E), which was primarily because of the snap-through mechanism of the bistable structure. Subsequently, the center part of the bistable structure collided with the ground, converting a large amount of energy into upward kinetic energy. As a result, the soft jumper attained a takeoff velocity of more than 2 m/s within 10 ms. The peak power density of the soft jumper calculated on the basis of the final takeoff velocity and the duration time (about 2 ms from t_0 to the takeoff moment) was up to 1000 W/kg. The takeoff velocity and the power density of the proposed bistable soft jumper even rivaled jumping insects in nature, such as *Phyotocoris varipes*, with an average velocity of 0.8 m/s and a power density of 225 W/kg (*47*).

We verified the influences of increasing magnetic field on the jumping height under different durations of an applied magnetic field (Fig. 3F). For each actuation time, the threshold of the magnetic field required to induce jumping was observed. Once the threshold was surpassed, the jumping height subsequently increased with an increase in the magnetic field. However, this tendency gradually slowed down because the capability of energy release of the bistable soft jumper reached its limit. On the other hand, elongating the actuating time of the magnetic field could lower the threshold of the critical magnetic field but had little effect on the final jumping height compared with the strength of the magnetic field. Further analysis of the material of the creases is shown in Fig. 3G, where we increased the proportion of PDMS in the silica gel to increase Young's modulus of creases (*48*). The sample stored more elastic potential energy because of the increase in Young's modulus of creases, which resulted in an increase in jumping height. Correspondingly, the threshold of the magnetic field required for triggering snap-through transition also increased because of the harder material.

Besides the parameters of the magnetic field, we also investigated the effect of size on the jumping height of the robot. On the basis of the standardized structure, a set of samples was prepared by proportional enlargement and reduction. Theoretically, the takeoff velocity is not dependent on size because the energy released through the snap-through transition is proportional to the mass (Supplementary

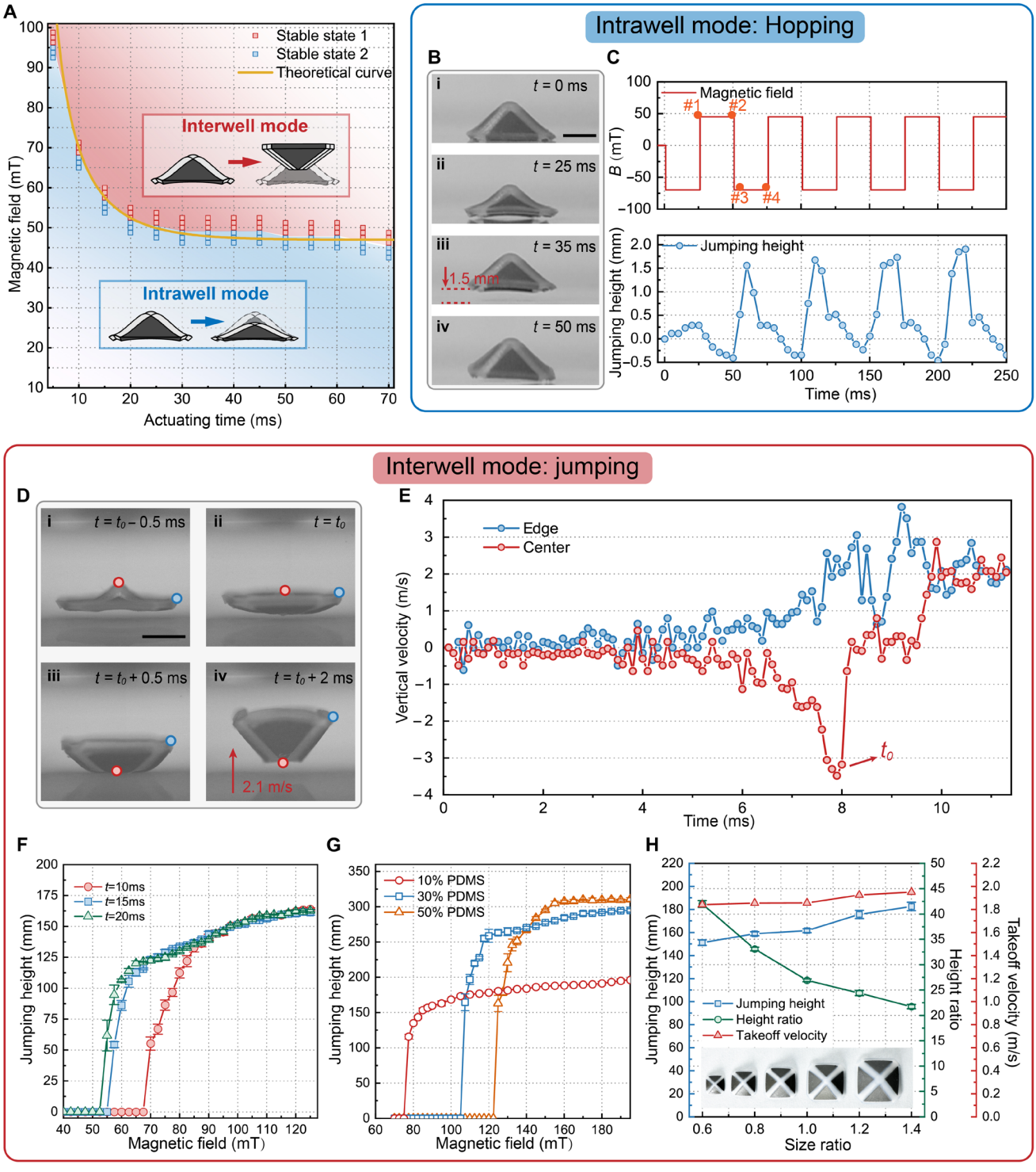

Fig. 3. Investigation of dynamic characteristics of the bistable soft jumper. (**A**) Parameter map of the stable state transition based on the strength and duration of the magnetic field and the theoretical curves. The intrawell mode and interwell mode can be divided according to the critical line. (**B**) Images of the detailed deformation under the intrawell mode of hopping. (**C**) The actuating magnetic field and the jumping heights of the bistable soft jumper during hopping. (**D**) Images of the detailed deformation under the interwell mode of jumping. t_0 is the critical moment when the center part reaches the maximum velocity. (**E**) The velocity of the edge and center parts of the robot as a function of time t. The magnetic field was activated when $t = 0$ ms. (**F**) Jumping heights of the bistable soft jumper as a function of the magnetic field strength upon different actuating time. Error bars represent SD ($N = 3$). (**G**) Comparison of jumping heights of robots with different materials of creases. The crease maintains a larger Young's modulus with a larger proportion of PDMS. Error bars represent SD ($N = 3$). (**H**) Comparison of jumping heights, height ratios, and takeoff velocities of the bistable soft jumpers with different sizes. Error bars represent SD ($N = 3$). Scale bars, 5 mm.

Methods). In a vacuum environment where air resistance is not taken into account, the same takeoff velocity leads to the same jumping height regardless of its size. However, in the real-world environment, bistable soft jumpers of different sizes are not affected by air resistance in the same way. A detailed theoretical analysis is given in Supplementary Methods, which summarizes that a smaller sample is more seriously affected by air resistance. Therefore, even with the same takeoff velocity, the smaller bistable soft jumper will reach a lower jumping height than the larger one. Our experimental results verified this theoretical hypothesis (Fig. 3H): There was about a 20% increase in jumping heights from the smallest sample (151 mm) to the largest sample (182 mm), whereas their respective takeoff velocities remained nearly the same with the maximum 5.6% deviation. Even so, the height ratio still had a notable increase, nearly doubling to 42 from 22. This conclusion demonstrated the potential applications of bistable soft jumpers at microscales. By reducing the structure size of the sample, the bistable soft jumper can enter confined spaces, such as within bodies or tubes while maintaining its jumping capability. On the basis of the strategy of scaling down the overall size of the robot to get a greater height ratio of jumping, we successfully fabricated a micro–bistable soft jumper with a total height of 2 mm that jumped more than 100 times its body height (Fig. 1C).

Control of bistable soft jumper

Controllability and consistency of the jumping direction are critical factors for practical applications. Among existing soft jumping robots, some lack the capability to jump directionally (*9*, *15*, *49*), whereas others require additional manipulation of the internal structures to realize jumping within restricted directions (*12*, *14*). This greatly reduces the adaptability of jumping robots for complex tasks.

In this work, the proposed bistable soft jumper had the ability to jump directionally (Fig. 4A). Figure 4B illustrates the principle of directional jumping in detail: The net magnetization M_{net}, which is composed of the individual magnetizations of the four magnetic panels, initially starts perpendicular to the ground. In the presence of the tilted magnetic field generated through the solid coil (fig. S4), M_{net} tends to align with the direction of the external magnetic field; thus, a rotational T is generated and causes the jumper to tilt during the snap-through transition. As a result, the bistable soft jumper is launched according to the direction of the magnetic field. Experiments were conducted to validate that the bistable soft jumper could perform jumps in any direction without additional manipulation. As shown in Fig. 4C, the bistable soft jumper performed eight jumps, with the starting point of each jump at the origin of the coordinates. By altering the direction of the magnetic field while maintaining a constant magnitude of the magnetic field, the bistable soft jumper was able to jump in eight different directions, each separated by 45° intervals around the circumference. The landing points of these eight jumps around the origin were recorded in Fig 4C. All eight jumps reached the same approximate jumping distance (60 mm), demonstrating that the bistable soft jumper had the ability to jump omnidirectionally under the guidance of the magnetic field.

In addition, we performed a quantitative analysis on the jumping distance of the bistable soft jumper in the same direction. The height of the bistable soft jumper used for the experiment was 6 mm, and the elastomer at its crease contained 10 wt % PDMS. The experimental results indicated that increasing the strength of the horizontal component of the magnetic field could effectively increase the jumping distance with the same strength as the vertical component of the magnetic field. However, when the horizontal component of the magnetic field was overly strong, the jumping distance began to decrease. As shown in Fig. 4D, the bistable soft jumper reached its maximum jumping distance of about 80 mm when the horizontal magnetic field increased to 32 mT. The jumping distance decreased as the horizontal magnetic field further increased. The reason was that the bistable soft jumper failed to sufficiently collide with the ground to acquire kinetic energy because of the excessive tilt during the actuating process. Acquiring the horizontal displacements came at the cost of vertical heights. The experiments indicated that with an increase in jumping distance, the jumping height gradually decreased.

To validate the ability to achieve controllable and precise jumping, we performed several implementations in practical scenarios. First, a stair-like obstacle with two platforms was provided, one with a height of 4 mm and the other with a height of 8 mm. According to the regularities analyzed in Fig 4D, the magnitudes of B_z and B_x were set to 150 and 20 mT, respectively, to obtain a high jumping trajectory to arrive at the higher platform. For the lower platform, increasing B_x to 37 mT while maintaining a constant B_z enabled the bistable soft jumper to follow a lower jumping trajectory. Furthermore, a set of hoops with heights of 85, 105, and 125 mm, respectively, was prepared. Here, the bistable soft jumper with a higher jumping height was used, which contained a higher proportion of PDMS (30 wt %) in the creases to store more elastic potential energy. Three loops were positioned at different angles to the bistable soft jumper. On the basis of the omnidirectional jumping demonstrated in Fig. 4C, the direction of the horizontal magnetic field B_r was adjusted to 135° away from the x axis to enable the bistable soft jumper to jump to the direction of the first loop. The magnitudes of B_z and B_r were set to 150 and 20 mT, respectively, to obtain the jumping trajectory with a height of about 125 mm and a distance of about 80 mm. For the remaining two loops, the direction of B_r was adjusted following the same principle. Last, the magnitude of B_r was increased to 27 and 35 mT, respectively, to achieve lower trajectories to jump through the loop of 105 mm and the loop of 85 mm. The above demonstrations show that the bistable soft jumper can be operated with controlled directions and trajectories.

Multiple locomotion modes in the pipeline for cleansing of dyed water

To demonstrate the use of the proposed bistable soft jumper for emerging applications in confined and complicated environments, we performed an application of water purification within a narrow pipeline. This application shows how the combination of high maneuverability, rapid responsiveness, and amphibious adaptability can all be demonstrated by the magnetic-driven bistable soft jumper.

We constructed a realistic environment of narrow pipes, demonstrating the potential of the proposed bistable soft jumper in such an application scenario (movie S3). First, the bistable soft jumper hopped to traverse the S-shaped pipeline. The direction of hopping could be guided by an external magnetic field that was applied in the form of a tilted alternating magnetic field. The frequency of the magnetic field was 40 Hz, under which the bistable soft jumper could move with a displacement of about 1 mm per cycle. High-frequency and small-amplitude displacements enabled

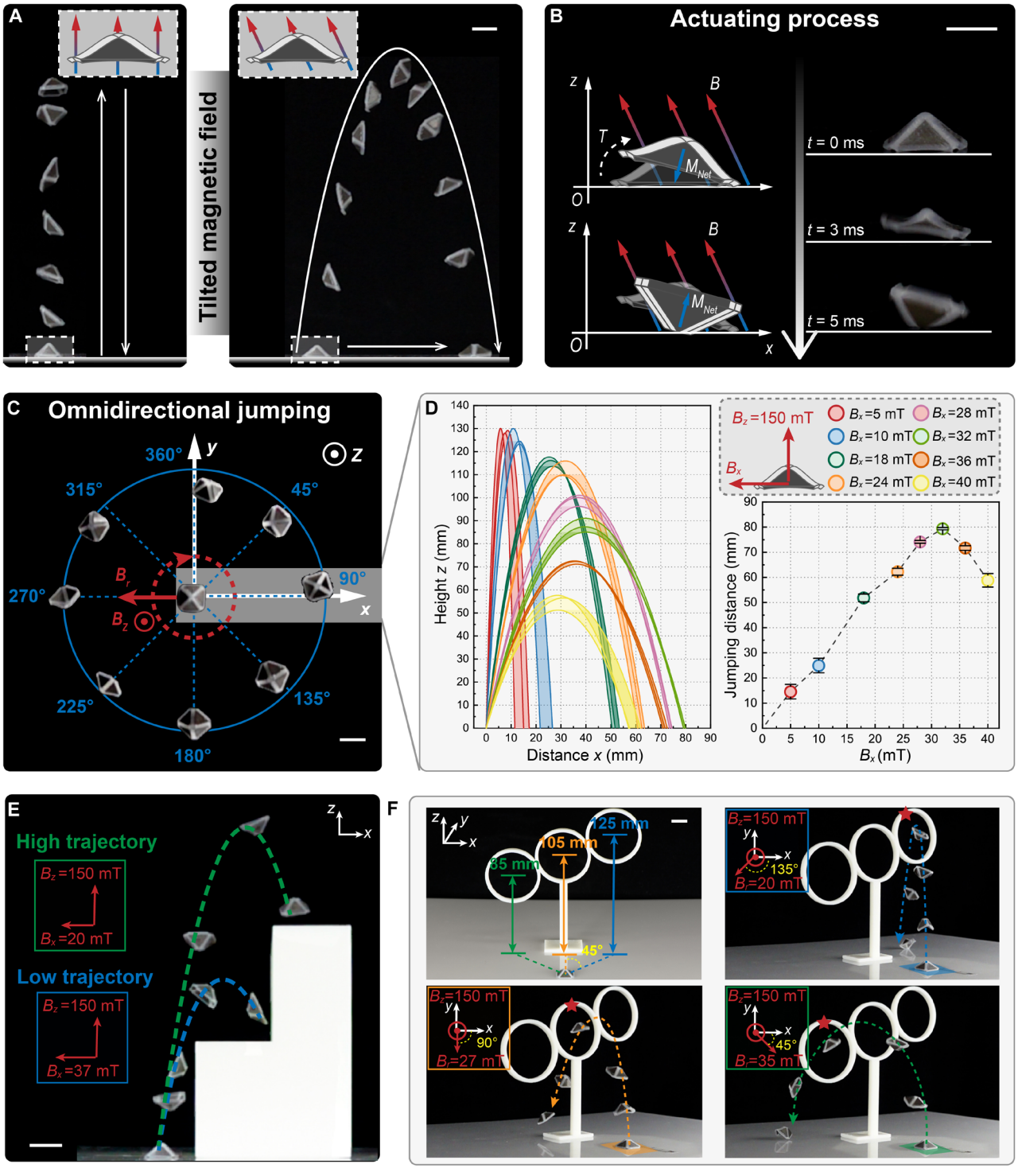

Fig. 4. Directional jumping of the bistable soft jumper. (**A**) Transition from jumping in place to directional jumping by tilting the magnetic field. (**B**) Mechanism and actuating process of the directional jumping. (**C**) Omnidirectional jumping (360°) of the bistable soft jumper. (**D**) Jumping trajectories under different values of B_x. The vertical component of the magnetic field remained at 150 mT, and the jumping distances were also analyzed as a function of B_x. Error bars represent SD ($N = 3$). (**E**) The bistable soft jumper could jump on different platforms by applying different trajectories. (**F**) The bistable soft jumper could jump through hoops at different distances and heights. The hoops were set at heights of 85, 105, and 125 mm. Scale bars, 10 mm.

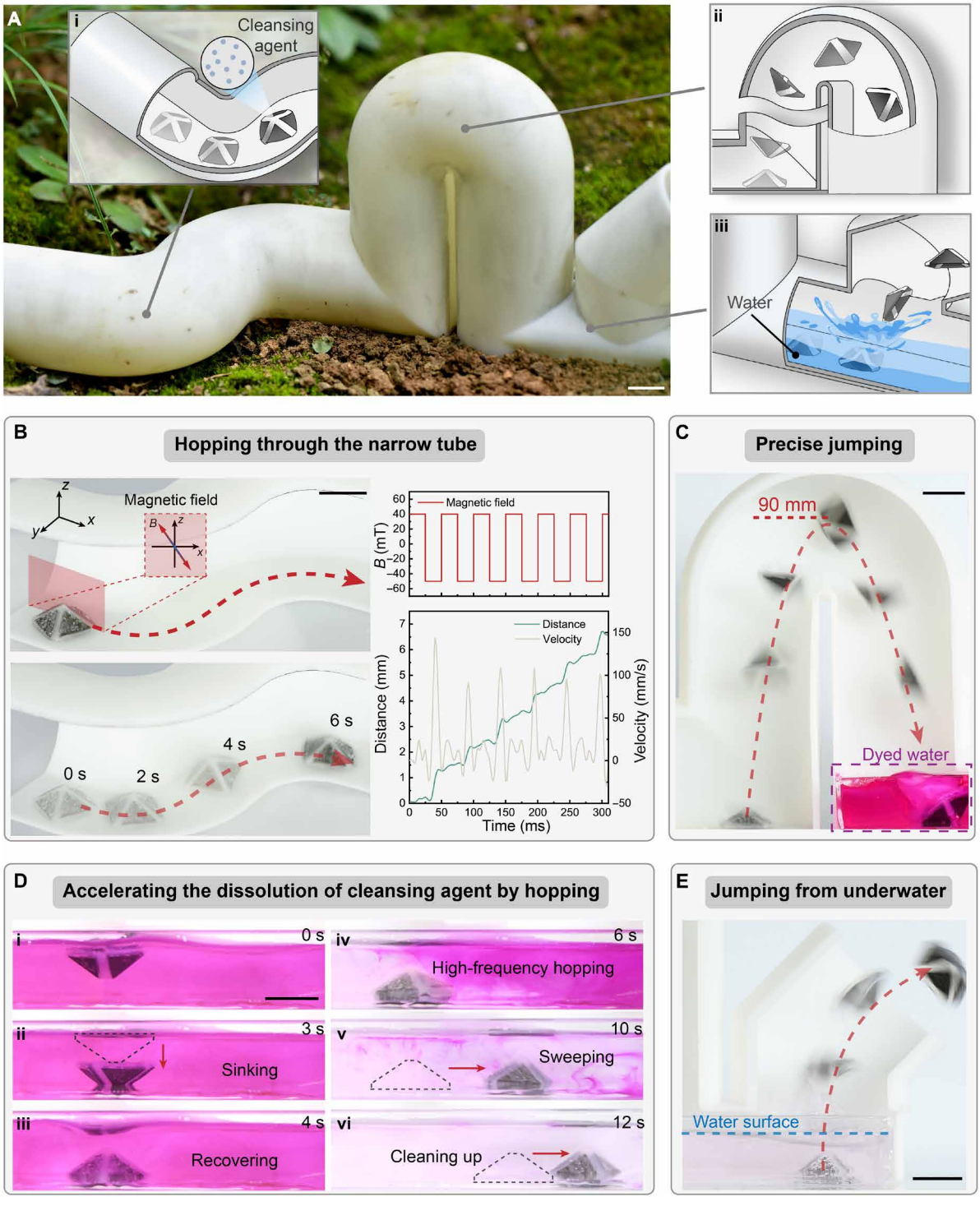

Fig. 5. Locomotion of bistable soft jumper in a pipeline. (**A**) Diagrams of the motion in a pipeline, including (i) hopping through the narrow tube, (ii) jumping through a U-shaped pipeline, and (iii) jumping from underwater. (**B**) Overlaid images indicating that the bistable soft jumper got through the tube by hopping. The displacement and velocity of the robot under the alternating magnetic field are shown. (**C**) Overlaid images indicating that the bistable soft jumper jumped precisely through the U-shaped pipeline. (**D**) The process of cleansing dyed water. (**E**) Overlaid images indicating that the bistable soft jumper jumped from underwater and left the pipeline. Scale bars, 10 mm.

the bistable soft jumper to precisely adjust its trajectory and effectively navigate around obstacles.

To get through the U-shaped pipeline, which maintained a nearly vertical wall, the bistable soft jumper switched to the interwell mode of jumping. As shown in Fig. 5C, the bistable soft jumper adopted a parabolic trajectory to traverse the U-shaped pipe with a height exceeding 15 times the bistable soft jumper's body height. Upon jumping through the U-shaped pipe, the bistable soft jumper fell into standing water that was colored with a purple dye. As shown in Fig. 5D, the bistable soft jumper managed to recover to its initial state by sinking to the bottom and performing a flip of the structure. Then, a cleansing agent was coated on the surface of the robot's surface. The high-frequency hopping could accelerate the release and reaction of the cleansing agent, causing the water to change from being purple to transparent. In addition, the bistable soft jumper swept through every region of the dyed water body to achieve comprehensive and effective purification of the dyed water.

Last, the bistable soft jumper jumped from the water after the task of water purification (Fig. 5E). The detailed procedure of jumping out of the water is elaborated in movie S6. Unlike in the air, the snap-through transition underwater was greatly hindered by the resistance of the water. However, benefiting from the ultrahigh power density of its bistable structure, the bistable soft jumper could still jump out of the water from a depth more than three times its height. In addition to the underwater resistance, the bistable soft jumper also encountered great resistance from the surface tension of the water. To address this, we designed a strategy to break the surface tension and reduce the contract area by actuating the bistable soft jumper to rotate (Supplementary Methods). Through the above experiments, we verified the potential of the bistable soft jumper to operate in both dry and aqueous environments.

DISCUSSION

Here, we demonstrate an ultrafast bistable soft jumper in a bistable structure that is wirelessly actuated by the magnetic field. By taking full advantage of the snap-through transition of the bistable structure, the bistable soft jumper can reach a maximum height of more than 100 times its body height while maintaining rapid response and recovery—rivaling the performance of jumping insects in nature. We also demonstrate the bistable soft jumper's unique ability to perform secondary locomotion of hopping by tuning the strength and duration of the magnetic field. In addition, precise control of the jumping trajectories—including directions, distances, and heights—can be realized. Compared with other types of soft jumpers, the bistable soft jumper proposed here shows superior environmental adaptability and locomotion capability. For its potential application, we also show a preliminary demonstration of the bistable soft jumper to pass through the complex pipeline and release a chemical agent to cleanse water, indicating the potential for operating in confined environments.

We anticipate that the proposed strategy of the bistable soft jumper can be scaled up or down to adapt to additional tasks. With the help of advanced manufacturing methods, applications of a downsized bistable soft jumper may extend to biomedical environments because the bistable mechanism can greatly enhance the locomotion capabilities of in vivo medical microrobots. In addition, the stable structure facilitates the integration of different components, such as probes, capsules for drug delivery, and other cargo. Besides magnetically driven robots, the bistable concept we propose may also be applicable to soft robots that are stimulated using other methods of actuation, including light- and temperature-responsive shape memory materials.

MATERIALS AND METHODS

Materials of the bistable soft jumper

The bistable soft jumper was composed of two parts: the deforming part and the actuating part. The deforming part was made of silica gels, which were a mix of PDMS (Dow Corning Sylgard 184) and Ecoflex 00-30 (Smooth-On, USA). The ratio between PDMS and Ecoflex 00-30 was adjusted to obtain deforming parts with different Young's moduli. The actuating part was made of magnetic materials, which were composed of PDMS and NdFeB microparticles (Jianghuai Ciye Corp.). The mass ratio of NdFeB microparticles and PDMS used here was selected as 3:1 to obtain the maximum magnetic moment density and Young's modulus. The magnetic material with a higher proportion of NdFeB microparticles was hard to cure and too brittle for practical use. The detailed material parameters can be found in table S6.

Fabrication of the bistable soft jumper

The fabrication of the bistable soft jumper can be simplified into five steps. The first step was stamping: The magnetic paste was prepared by mixing the PDMS (Dow Corning Sylgard 184) and NdFeB microparticles (Jianghuai Ciye Corp.) at a mass ratio of 1:3. These components were thoroughly mixed by a planetary mixer (AR-100, THINKY Corp., Tokyo, Japan) at 2000 rpm for 2 min and then defoamed at 2000 rpm for 2 min. Then, the magnetic paste was scraped into the mold (laser-cut aluminum sheet) to shape it into the required sizes. The second step was curing: After the magnetic paste completely filled the cavities of the mold, the mold was placed in the oven and heated at 120°C for 30 min to cure the magnetic paste. The third step was magnetization: The cured magnetic panels were magnetized in a high-intensity magnetic field B_m (3 T) generated by a magnetizer (JH12160) to program the magnetic polarities of the NdFeB microparticles. The fourth step was pouring: The magnetic panels were precisely pasted on the surface of the bottom mold with the help of a double-sided tape (3M). Then, the silica gels mixed with Ecoflex 00-30 and PDMS were poured into the bottom mold to submerge the fixed magnetic panels. The fifth step was casting: After a 10-min defoaming procedure to eliminate the internal bubbles of the silica gels, the bottom mold was paired with the top mold to eject the excess silica gels and cast the shape of the bistable soft jumper. Upon the full curing of the silica gels, the mold was opened to retrieve the sample, and further trimming was needed to complete the fabrication of the bistable soft jumper.

Control method of the magnetic field

The magnetic field pulse was controlled by dc motor drivers (SyRen 50A, Dimension Engineering). The dc motor driver was powered by a 24-V power supply (24 V, 62.5 A, S-1500-24, MEAN WELL), and its output ports were connected to the electromagnetic coils. The driver controlled the voltage of the coils on the basis of the signal transmitted by the Arduino PWM (pulse width modulation) output ports. The signal value ranged from −127 to 127, which corresponded to the output voltage in the range of −24 to 24 V. Before

conducting experiments, we measured the maximum intensity of the magnetic field that could be generated by electromagnetic coils (when the input voltage was 24 V). During experiments, the Arduino PWM calculated the required output voltage on the basis of the user-input intensity of the magnetic field because the intensity of the magnetic field exhibited a linear relationship with the voltage. Last, the corresponding signal values, including output voltage and duration, were transmitted to the DC motor drivers to output the desired magnetic field pulse.

Two types of electromagnetic coils were used here: The first coil set was the Helmholtz coil, which provided a region with a nearly uniform magnetic field. The second coil set was the solid electromagnetic coil, which contained a piece of silicon alloy steel (DWSi3) in the middle of the circular wires. The specific configurations and properties of the two coil sets are analyzed in Supplementary Methods.

FEA of the bistable soft jumper

The FEA of the bistable soft jumper was carried out in the commercial FEA software ABAQUS. The magnetic parts of the bistable soft jumper tend to align with the magnetic field and drive the transformation of the whole structure. The constitutional model was established to analyze the whole deformation of the bistable structure. The magnetic soft material was considered to follow the adapted neo-Hookean constitutive model (*35*, *37*), and the total potential energy per unit volume of the magnetic material was expressed as

$$W = \frac{G}{2}\left(J^{-\frac{2}{3}}I_1 - 3\right) + \frac{K}{2}(J-1)^2 - \mathbf{FM}\cdot\mathbf{B} \quad (4)$$

where G is the shear modulus of the material and K is the bulk modulus. $I_1 = \mathrm{tr}(\mathbf{F}^T\mathbf{F})$ is the first invariant of the left Cauchy-Green tensor, where $\mathbf{F}$ represents the deformation gradient tensor. J is defined as the volumetric Jacobian of $\mathbf{F}$ by $J = \det\mathbf{F}$. $\mathbf{M}$ is the magnetic moment density of a unit in the reference coordinate, and $\mathbf{B}$ is the external magnetic field applied to the magnetic material.

On the basis of Eq. 4, the Cauchy stress tensor σ was calculated as

$$\sigma = \frac{1}{J}\frac{\partial W}{\partial \mathbf{F}}\mathbf{F}^T = GJ^{-\frac{5}{3}}\left(\mathbf{F}\mathbf{F}^T - \frac{I_1}{3}\mathbf{I}\right) + K(J-1)\mathbf{I} - \frac{1}{J}\mathbf{B}\otimes\mathbf{FM} \quad (5)$$

where $\mathbf{I}$ is the identity tensor and $\otimes$ denotes the dyadic product. Equation 5 describes the stress tensor in terms of the elastic contribution $GJ^{-\frac{5}{3}}\left(\mathbf{F}\mathbf{F}^T - \frac{I_1}{3}\mathbf{I}\right) + K(J-1)\mathbf{I}$ and the magnetic contribution $\frac{1}{J}\mathbf{B}\otimes\mathbf{FM}$. If $\mathbf{B}$ is aligned with $\mathbf{FM}$ in the current state, then the magnetic contribution vanishes.

The user-element subroutine developed by Kim and colleagues (*37*) was applied to facilitate the simulation of the bistable soft jumper. The bistable soft jumper consisted of two different materials: silica gels and magnetic materials. The material parameters, including Young's modulus E, G, K, $\mathbf{M}$, and $\mathbf{B}$, were prescribed in the input file. For the silica gels, we adjusted E by mixing different proportions of PDMS into Ecoflex 00-30. The Young's moduli of silica gels ranged from 70 to 600 kPa (table S1). The Young's modulus of the magnetic material used here was about 4.6 MPa, which was much larger than that of the silica gels. The large difference between Young's modulus values led to the strain in the deformation being mainly concentrated in the silica gels (at the crease). The G of the material was determined by

$$G = \frac{E}{2(1+\mu)} \quad (6)$$

where Poisson's ratio μ was set to 0.49. K was chosen to satisfy $K = 1000E$ to approximate near incompressibility. The $\mathbf{M}$ of 75 wt % NdFeB magnetic materials was measured to be about 180 kA/m, whereas the $\mathbf{M}$ of the silica gels was 0 kA/m because of the absence of magnetic particles. Accordingly, the magnetic materials were the main source of the magnetic torque that triggered the snap-through transition. The uniform $\mathbf{B}$ applied for actuation was also defined in the input file.

The quarter of the whole structure was modeled to reduce computation. The structure was then divided into sets of elements on the basis of their respective materials, with each set given the corresponding material parameters. The boundary condition of the edge was set as Z symmetry (U3 = UR1 = UR2 = 0), which prohibited any displacement or rotation in the Z axis. The stimulus of the simulation was the magnetic field. Once the simulation procedure was started, ABAQUS iterated until convergence on the basis of the input magnetic field parameters and the magnetic moment density of materials. To ensure convergence during the intense snap-through process, automatic stabilization was implemented with a specified damping factor of 0.0002. The simulations of deformation were consistent with the experiments. By analyzing the strain energy in the simulation results, we plotted the potential energy curve of the structure as it deformed.

Statistical analysis

Experimental values were obtained by conducting measurements N times, and the results were reported in the figures as means ± SD. For experiments involving a single measurement ($N = 1$), only the raw measurement values were reported. The regression analysis was performed to evaluate the deviation between the simulated deformation and the experimental deformation.

Supplementary Materials

The PDF file includes:

Methods
Figs. S1 to S17
Tables S1 to S8

Other Supplementary Material for this manuscript includes the following:

Movies S1 to S8

REFERENCES AND NOTES

1. F. J. Larabee, A. V. Suarez, Mandible-powered escape jumps in trap-jaw ants increase survival rates during predator-prey encounters. *PLOS One* **10**, e0124871 (2015).
2. W. E. Cooper, Risk factors and escape strategy in the grasshopper *Dissosteira carolina*. *Behaviour* **143**, 1201–1218 (2006).
3. G. Hoyle, The leap of the grasshopper. *Sci. Am.* **198**, 30–35 (1958).
4. E. W. Hawkes, C. Xiao, R.-A. Peloquin, C. Keeley, M. R. Begley, M. T. Pope, G. Niemeyer, Engineered jumpers overcome biological limits via work multiplication. *Nature* **604**, 657–661 (2022).
5. D. W. Haldane, M. M. Plecnik, J. K. Yim, R. S. Fearing, Robotic vertical jumping agility via series-elastic power modulation. *Sci. Robot.* **1**, eaag2048 (2016).
6. Z. Zhakypov, K. Mori, K. Hosoda, J. Paik, Designing minimal and scalable insect-inspired multi-locomotion millirobots. *Nature* **571**, 381–386 (2019).
7. M. Kovac, M. Fuchs, A. Guignard, J.-C. Zufferey, D. Floreano, A miniature 7g jumping robot, in *2008 IEEE International Conference on Robotics and Automation* (IEEE, 2008), pp. 373–378.
8. G.-P. Jung, C. S. Casarez, S.-P. Jung, R. S. Fearing, K.-J. Cho, An integrated jumping-crawling robot using height-adjustable jumping module, in *2016 IEEE International Conference on Robotics and Automation (ICRA)* (IEEE, 2016), pp. 4680–4685.

9. M. Duduta, F. Berlinger, R. Nagpal, D. R. Clarke, R. J. Wood, F. Z. Temel, Tunable multi-modal locomotion in soft dielectric elastomer robots. *IEEE Robot. Autom. Lett.* **5**, 3868–3875 (2020).
10. M. Duduta, F. Berlinger, R. Nagpal, D. Clarke, R. Wood, F. Z. Temel, Electrically-latched compliant jumping mechanism based on a dielectric elastomer actuator. *Smart Mater. Struct.* **28**, 09LT01 (2019).
11. R. Chen, Z. Yuan, J. Guo, L. Bai, X. Zhu, F. Liu, H. Pu, L. Xin, Y. Peng, J. Luo, Y. Sun, Legless soft robots capable of rapid, continuous, and steered jumping. *Nat. Commun.* **12**, 7028 (2021).
12. C. Ahn, X. Liang, S. Cai, Bioinspired design of light-powered crawling, squeezing, and jumping untethered soft robot. *Adv. Mater. Technol.* **4**, 1900185 (2019).
13. H. Guo, A. Priimagi, H. Zeng, Optically controlled latching and launching in soft actuators. *Adv. Functional Mater.* **32**, 2108919 (2022).
14. J. Hu, Z. Nie, M. Wang, Z. Liu, S. Huang, H. Yang, Springtail-inspired light-driven soft jumping robots based on liquid crystal elastomers with monolithic three-leaf panel fold structure. *Angew. Chem. Int. Ed. Engl.* **62**, e202218227 (2023).
15. Y. Hu, J. Liu, L. Chang, L. Yang, A. Xu, K. Qi, P. Lu, G. Wu, W. Chen, Y. Wu, Electrically and sunlight-driven actuator with versatile biomimetic motions based on rolled carbon nanotube bilayer composite. *Adv. Funct. Mater.* **27**, 1704388 (2017).
16. N. W. Bartlett, M. T. Tolley, J. T. Overvelde, J. C. Weaver, B. Mosadegh, K. Bertoldi, G. M. Whitesides, R. J. Wood, A 3D-printed, functionally graded soft robot powered by combustion. *Science* **349**, 161–165 (2015).
17. M. T. Tolley, R. F. Shepherd, M. Karpelson, N. W. Bartlett, K. C. Galloway, M. Wehner, R. Nunes, G. M. Whitesides, R. J. Wood, An untethered jumping soft robot, in *2014 IEEE/RSJ International Conference on Intelligent Robots and Systems* (IEEE, 2014), pp. 561–566.
18. G.-H. Jeon, Y.-J. Park, Soft jumping robot using soft morphing and the yield point of magnetic force. *Appl. Sci.* **11**, 5891 (2021).
19. A. Rajappan, B. Jumet, D. J. Preston, Pneumatic soft robots take a step toward autonomy. *Sci. Robot.* **6**, eabg6994 (2021).
20. Z. Liu, J. Liu, H. Wang, X. Yu, K. Yang, W. Liu, S. Nie, W. Sun, Z. Xie, B. Chen, A 1-mm-thick miniatured mobile soft robot with mechanosensation and multimodal locomotion. *IEEE Robot. Automat. Lett.* **5**, 3291–3298 (2020).
21. F. Zhai, Y. Feng, Z. Li, Y. Xie, J. Ge, H. Wang, W. Qiu, W. Feng, 4D-printed untethered self-propelling soft robot with tactile perception: Rolling, racing, and exploring. *Matter* **4**, 3313–3326 (2021).
22. D. Tang, C. Zhang, H. Sun, H. Dai, J. Xie, J. Fu, P. Zhao, Origami-inspired magnetic-driven soft actuators with programmable designs and multiple applications. *Nano Energy* **89**, 106424 (2021).
23. W. Hu, G. Z. Lum, M. Mastrangeli, M. Sitti, Small-scale soft-bodied robot with multimodal locomotion. *Nature* **554**, 81–85 (2018).
24. S. Wu, C. M. Hamel, Q. Ze, F. Yang, H. J. Qi, R. Zhao, Evolutionary algorithm-guided voxel-encoding printing of functional hard-magnetic soft active materials. *Adv. Intel. Syst.* **2**, 2000060 (2020).
25. Q. Ze, S. Wu, J. Nishikawa, J. Dai, Y. Sun, S. Leanza, C. Zemelka, L. S. Novelino, G. H. Paulino, R. R. Zhao, Soft robotic origami crawler. *Sci. Adv.* **8**, eabm7834 (2022).
26. S. Chen, Y. Cao, M. Sarparast, H. Yuan, L. Dong, X. Tan, C. Cao, Soft crawling robots: Design, actuation, and locomotion. *Adv. Mater. Technol.* **5**, 1900837 (2020).
27. T. Xu, J. Zhang, M. Salehizadeh, O. Onaizah, E. Diller, Millimeter-scale flexible robots with programmable three-dimensional magnetization and motions. *Sci. Robot.* **4**, eaav4494 (2019).
28. Y. Wang, P. Zhang, H. Huang, J. Zhu, Bio-inspired transparent soft jellyfish robot. *Soft Robot.* **10**, 590–600 (2023).
29. C. Yin, F. Wei, S. Fu, Z. Zhai, Z. Ge, L. Yao, M. Jiang, M. Liu, Visible light-driven jellyfish-like miniature swimming soft robot. *ACS Appl. Mater. Interfaces* **13**, 47147–47154 (2021).
30. Y. Wu, J. K. Yim, J. Liang, Z. Shao, M. Qi, J. Zhong, Z. Luo, X. Yan, M. Zhang, X. Wang, Insect-scale fast moving and ultrarobust soft robot. *Sci. Robot.* **4**, eaax1594 (2019).
31. J. Wang, T. Zhao, Y. Fan, H. Wu, J. A. Lv, Leveraging Bioinspired Structural constraints for tunable and programmable snapping dynamics in high-speed soft actuators. *Adv. Funct. Mater.* **33**, 2209798 (2023).
32. J. T. Overvelde, T. Kloek, J. J. D'haen, K. Bertoldi, Amplifying the response of soft actuators by harnessing snap-through instabilities. *Proc. Natl. Acad. Sci. U.S.A.* **112**, 10863–10868 (2015).
33. N. Hu, R. Burgueño, Buckling-induced smart applications: Recent advances and trends. *Smart Mater. Struct.* **24**, 063001 (2015).
34. J. Jeon, J.-C. Choi, H. Lee, W. Cho, K. Lee, J. G. Kim, J.-W. Lee, K.-I. Joo, M. Cho, H.-R. Kim, Continuous and programmable photomechanical jumping of polymer monoliths. *Mater. Today* **49**, 97–106 (2021).
35. Y. Kim, H. Yuk, R. Zhao, S. A. Chester, X. Zhao, Printing ferromagnetic domains for untethered fast-transforming soft materials. *Nature* **558**, 274–279 (2018).
36. C. Zhang, X. Li, L. Jiang, D. Tang, H. Xu, P. Zhao, J. Fu, Q. Zhou, Y. Chen, 3D printing of functional magnetic materials: From design to applications. *Adv. Funct. Mater.* **31**, 2102777 (2021).
37. R. Zhao, Y. Kim, S. A. Chester, P. Sharma, X. Zhao, Mechanics of hard-magnetic soft materials. *J. Mech. Phys. Solids* **124**, 244–263 (2019).
38. Y. Kim, X. Zhao, Magnetic soft materials and robots. *Chem. Rev.* **122**, 5317–5364 (2022).
39. V. Ramachandran, M. D. Bartlett, J. Wissman, C. Majidi, Elastic instabilities of a ferroelastomer beam for soft reconfigurable electronics. *Extreme Mech. Lett.* **9**, 282–290 (2016).
40. L. Chen, K. Tan, S. Yang, Q. Deng, Evoking the snap-through instability in hard-magnetic soft materials: Rapid actuation and giant deformation. *Int. J. Solids Structures* **246**, 111607 (2022).
41. X. Hou, Y. Liu, G. Wan, Z. Xu, C. Wen, H. Yu, J. X. Zhang, J. Li, Z. Chen, Magneto-sensitive bistable soft actuators: Experiments, simulations, and applications. *Appl. Phys. Lett.* **113**, 221902 (2018).
42. A. Amor, A. Fernandes, J. Pouget, Snap-through of elastic bistable beam under contactless magnetic actuation. *Int. J. Non-Linear Mech.* **119**, 103358 (2020).
43. Y. Chi, Y. Li, Y. Zhao, Y. Hong, Y. Tang, J. Yin, Bistable and multistable actuators for soft robots: Structures, materials, and functionalities. *Adv. Mater.* **34**, 2110384 (2022).
44. J. A. Faber, A. F. Arrieta, A. R. Studart, Bioinspired spring origami. *Science* **359**, 1386–1391 (2018).
45. Z. Kala, M. Kalina, Static equilibrium states of von mises trusses. *Int. J. Mech. Sci.* **10**, 294–298 (2016).
46. F. O. Falope, M. Pelliciari, L. Lanzoni, A. M. Tarantino, Snap-through and Eulerian buckling of the bi-stable von Mises truss in nonlinear elasticity: A theoretical, numerical and experimental investigation. *Int. J. Non-Linear Mech.* **134**, 103739 (2021).
47. M. Burrows, M. Dorosenko, Jumping performance of flea hoppers and other mirid bugs (Hemiptera, Miridae). *J. Exp. Biol.* **220**, 1606–1617 (2017).
48. J. Vaicekauskaite, P. Mazurek, S. Vudayagiri, A. L. Skov, Mapping the mechanical and electrical properties of commercial silicone elastomer formulations for stretchable transducers. *J. Mater. Chem. C* **8**, 1273–1279 (2020).
49. W. A. Churaman, A. P. Gerratt, S. Bergbreiter, First leaps toward jumping microrobots, in *2011 IEEE/RSJ International Conference on Intelligent Robots and Systems* (IEEE, 2011), pp. 1680–1686.
50. Y. Kim, J. van den Berg, A. J. Crosby, Autonomous snapping and jumping polymer gels. *Nat. Mater.* **20**, 1695–1701 (2021).
51. Y. Jiang, L. M. Korpas, J. R. Raney, Bifurcation-based embodied logic and autonomous actuation. *Nat. Commun.* **10**, 128 (2019).
52. K. Yu, X. Ji, T. Yuan, Y. Cheng, J. Li, X. Hu, Z. Liu, X. Zhou, L. Fang, Robust jumping actuator with a shrimp-shell architecture. *Adv. Mater.* **33**, 2104558 (2021).
53. H. Lee, C. Xia, N. X. Fang, First jump of microgel; actuation speed enhancement by elastic instability. *Soft Matter* **6**, 4342–4345 (2010).
54. M. Li, X. Wang, B. Dong, M. Sitti, In-air fast response and high speed jumping and rolling of a light-driven hydrogel actuator. *Nat. Commun.* **11**, 3988 (2020).
55. H. Arazoe, D. Miyajima, K. Akaike, F. Araoka, E. Sato, T. Hikima, M. Kawamoto, T. Aida, An autonomous actuator driven by fluctuations in ambient humidity. *Nat. Mater.* **15**, 1084–1089 (2016).
56. W. Fan, C. Shan, H. Guo, J. Sang, R. Wang, R. Zheng, K. Sui, Z. Nie, Dual-gradient enabled ultrafast biomimetic snapping of hydrogel materials. *Sci. Adv.* **5**, eaav7174 (2019).
57. J. Sun, B. Tighe, J. Zhao, Tuning the energy landscape of soft robots for fast and strong motion, in *2020 IEEE International Conference on Robotics and Automation (ICRA)* (IEEE, 2020), pp. 10082–10088.
58. B. Gorissen, D. Melancon, N. Vasios, M. Torbati, K. Bertoldi, Inflatable soft jumper inspired by shell snapping. *Sci. Robot.* **5**, eabb1967 (2020).
59. F. Ni, D. Rojas, K. Tang, L. Cai, T. Asfour, A jumping robot using soft pneumatic actuator, in *2015 IEEE International Conference on Robotics and Automation (ICRA)* (IEEE, 2015), pp. 3154–3159.
60. C. Hong, Z. Ren, C. Wang, M. Li, Y. Wu, D. Tang, W. Hu, M. Sitti, Magnetically actuated gearbox for the wireless control of millimeter-scale robots. *Sci. Robot.* **7**, eabo4401 (2022).
61. Y. Wang, X. Du, H. Zhang, Q. Zou, J. Law, J. Yu, Amphibious miniature soft jumping robot with on-demand in-flight maneuver. *Adv. Sci.* **10**, 2207493 (2023).

Acknowledgments: We thank X. Ni, Z. Hu, and members of the ZPLab for valuable assistance in conducting the experiments. We also thank C. Lyu for proofreading the manuscript. **Funding:** This work was supported in part by the National Natural Science Foundation of China under grant 52205424, the Zhejiang Provincial Natural Science Foundation of China under grant LY23A020001, and the "Pioneer" and "Leading Goose" R&D Program of Zhejiang Province under grant 2023C01170. **Author contributions:** Conceptualization: D.T., C.Z., and P.Z. Methodology: D.T., C.Z., C.P., and C.M. Investigation: D.T., H.H., H.D., and H.S. Funding acquisition: P.Z., C.Z., and J.F. Project administration: P.Z., C.Z., and C.P. Supervision: P.Z. and C.M. Writing—original draft: D.T. Writing—review and editing: C.M., C.P., C.Z., and P.Z. **Competing interests:** The authors declare that they have no competing interests. **Data and materials availability:** All data needed to evaluate the conclusions in the paper are presented in the paper or the Supplementary Materials and are available online at https://doi.org/10.5061/dryad.hdr7sqvsg.

Submitted 10 November 2023
Accepted 22 July 2024
Published 21 August 2024
10.1126/scirobotics.adm8484

Science Robotics

Bistable soft jumper capable of fast response and high takeoff velocity

Daofan Tang, Chengqian Zhang, Chengfeng Pan, Hao Hu, Haonan Sun, Huangzhe Dai, Jianzhong Fu, Carmel Majidi, and Peng Zhao

Sci. Robot. **9** (93), eadm8484. DOI: 10.1126/scirobotics.adm8484

Editor's summary

For jumping to be an efficient mode of locomotion, it requires a high power output and fast response time, which can be difficult to achieve in soft materials. Here, Tang *et al*. developed a pyramid-shaped soft jumper with a fast snap-through transition triggered by a magnetic field. Made of magnetic panels and elastomer creases, the robot rapidly transitions from the top of the pyramid pointing up to pointing down, propelling the robot upward to more than 100 times its height. By adjusting the strength, duration, and direction of the magnetic field, the robot's movement can go from jumping to hopping, and its trajectory can be controlled, allowing it to navigate through confined spaces such as a pipeline. —Melisa Yashinski